CHAPTER FOUR

Electron Transfer Behaviour of Single-Walled Carbon Nanotubes Electro-Decorated with Nickel and Nickel Oxide Layers and Its Electrocatalysis Towards Diethylaminoethanethiol (DEAET): An Adsorption-Controlled Electrode Process*

* The following publications resulted from part of the research work presented in this chapter and they are not referenced further in this thesis:

2. **Abolanle S. Adekunle**, Kenneth I. Ozoemena, *Electrochim. Acta* 53 (2008) 5774-5782.
3. **Adekunle A. S.**, Pillay J., Ozoemena K. I., *Electroanalysis* 20 (2008) 2587-2591.

4.1 FTIR, SEM images and EDX characterisation

Figure 4.1 shows the comparative Fourier transformed infra-red (FTIR) spectra of the pristine (a) and acid-treated SWCNTs (b).

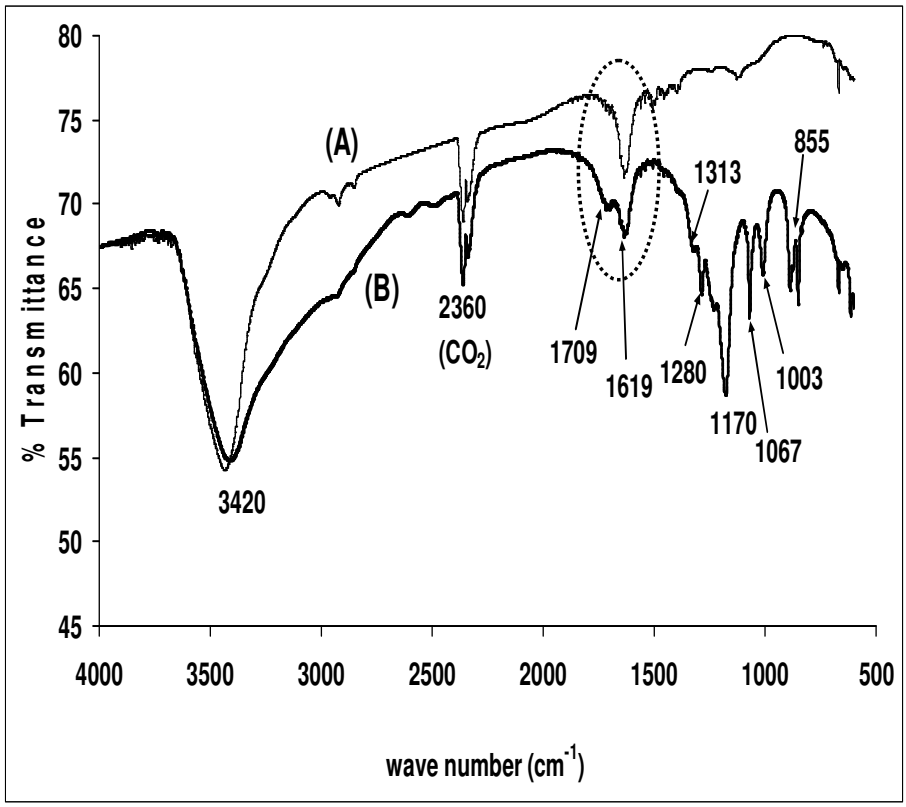

Figure 4.1: Comparative FTIR of pristine SWCNTs (a) and acid-treated SWCNTs (b).

An intense band at 3420 cm^{-1} was obseved for the pristine SWCNT which is attributed to OH group, possibly due to moisture absorption of the pristine. This is in agreement with the observation of Martinez et al. [1] that even the untreated SWCNTs do contain some functional groups. The acid treated species (b) gave a very broad band in the 3420 cm^{-1} region compared to the pristine SWCNTs, clearly indicating the presence of -OH stretching of the COOH group. Both species gave vibrational modes corresponding to C=C bonds at 1619 cm^{-1}, assigned to the nanotube phonon modes. More

importantly, after the acid treatment (b), a new band appeared at 1704 cm^{-1} due to the C=O of the COOH groups. The diminished intensity of the band at 1619 cm^{-1} for the acid-treated compared to that of the pristine SWCNTs is a clear indication that some of the C=C bands have now been functionalized with COOH groups. The sharp band at 1170 cm^{-1} is ascribed to the thiocarbonyl (C-S) [2]. The bands at the 1067 and a shoulder at 1003 cm^{-1} are ascribed to the asymmetric and symmetric stretching modes of SO_3, respectively. These S=O stretching modes resulted from the formation of hydrated sulfonic acid group ($SO_3^-H^+$ H_2O) due to the presence of trace water. The presence of these sulphur groups is clearly visible in the EDX spectra (Figure 4.2). The bands near 855 cm^{-1} regions are due C-H bending, while those at the 1280 and 1313 cm^{-1} are assigned to the O-C. The peak at 3460 cm^{-1}, with similar intensity for both pristine and acid-treated SWCNTs, is ascribed to the interfering CO_2, possibly arising from the nitrogen gas purge boxes of the FTIR experimental setup. No attempt was made to experimentally quantify the extent of carboxylation of the SWCNTs. However, as clearly indicated in the Wang et al. [3], it is known that the procedure employed in the carboxylation process generally give solubility ≤0.08mg of SWCNTs ml^{-1} of solvent. It is reported [3] that the use of microwave strategy that resulted in stable concentrations as high as 10mg SWCNTs ml^{-1} in deionized water, which is approximately two orders of magnitude higher than those obtained using similar strategies. Wang et al. [3] also reported that 33.3% of the carbon atoms on the SWCNTs backbone were carboxylated. From this report, it could be easily be inferred that the extent of carboxylation used in this work could not be more than 0.5%.

Figure 4.2 exemplifies FESEM images of the EPPGE (a), EPPGESWCNT (b), EPPGE-SWCNT-Ni (c) and EPPGE-SWCNT-NiO (d).

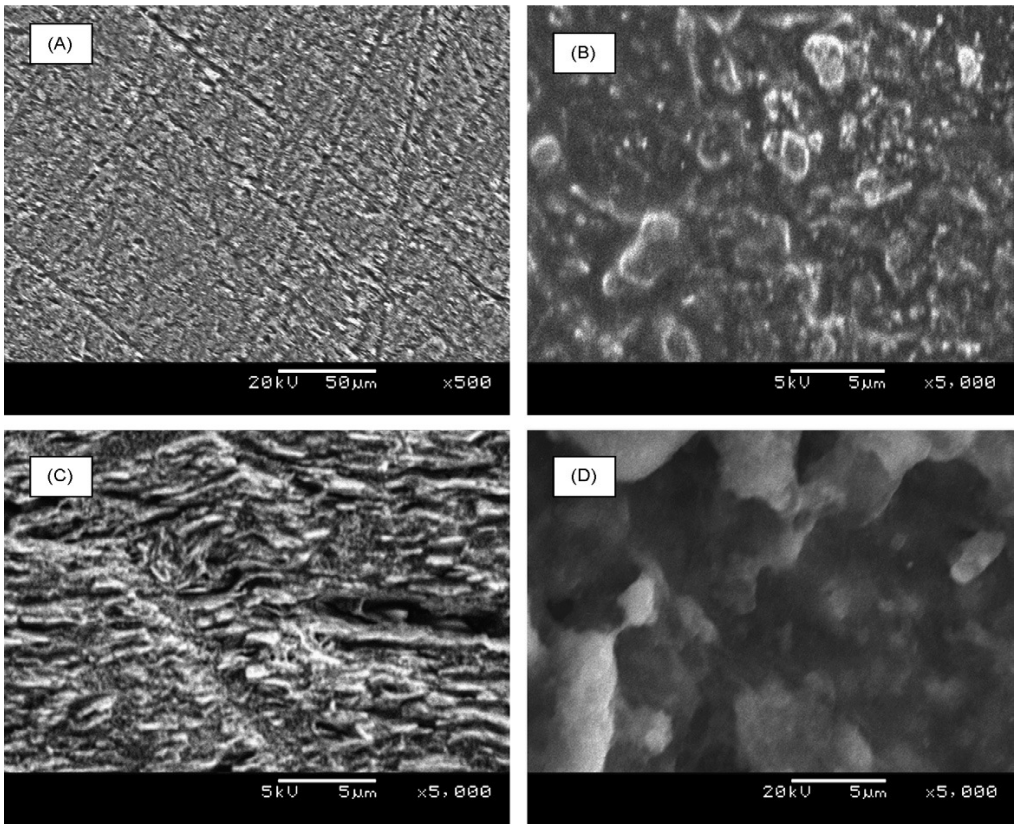

Figure 4.2: FESEM images of bare EPPGE (a), EPPGE-SWCNT (b), EPPGE-SWCNT-Ni (c) and EPPGE-SWCNT-NiO (d). The size bars are 50 µm for (a) and 5 µm for (b)–(d).

The results indicate that the original edge-plane surface of the EPPGE (a) is replaced with aggregated acid-treated SWCNTs (b), and upon introduction of the nickel particles an interconnected layer-structured network image of the SWCNT-modified EPPGE (c) was observed. However, upon electrochemical treatment in aqueous solution these layer-structured networks (c) are disconnected transforming to lumps with exposed interior (d), with sizes in the micrometer ranges. Like other reports on CNTs containing metal or

metal oxide impurities [4], it may be reasonable to speculate here that these nickel particles are either trapped in the graphite layers and/or located on the outside of the tubes exposed to the solutions, and/or mixed amongst the bundles of the SWCNT.

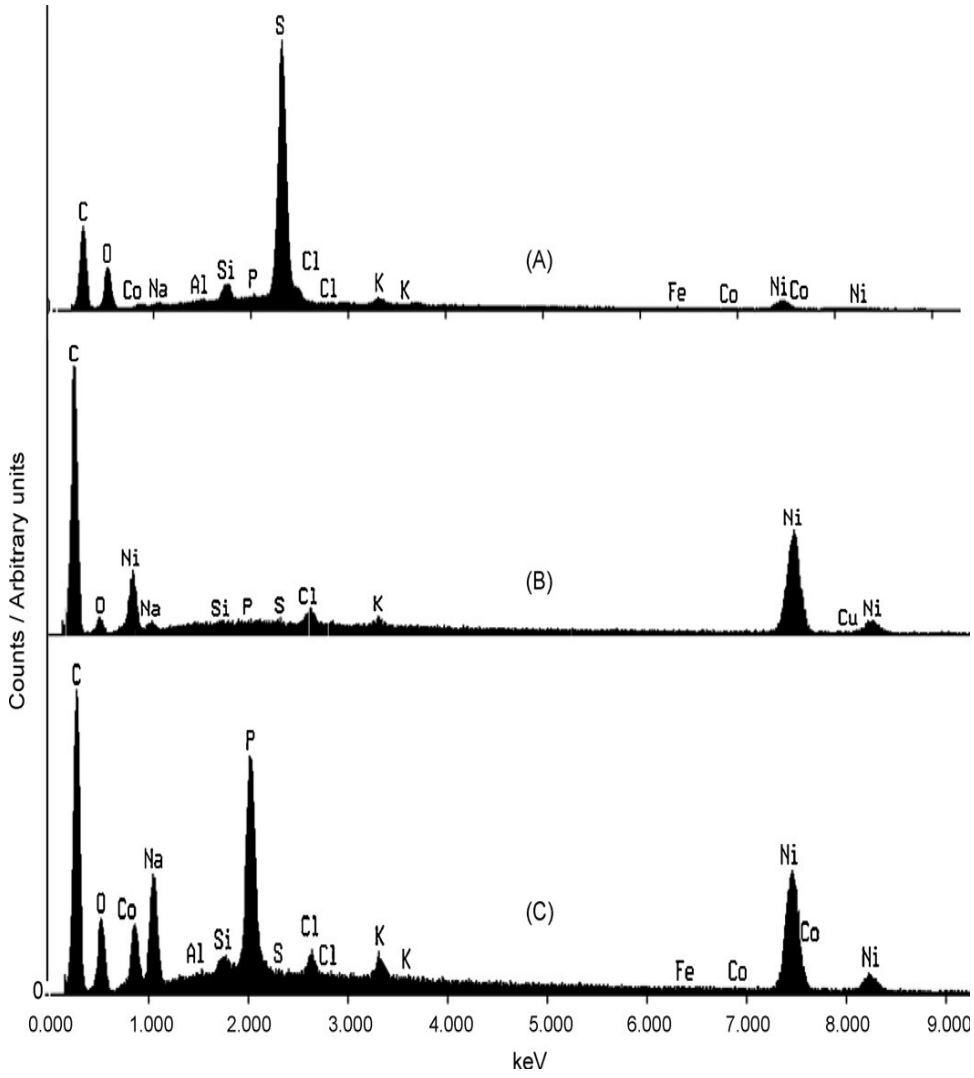

Figure 4.3: EDX spectra of (a) EPPGE-SWCNT, (b) EPPGE-SWCNT-Ni, and (c) EPPGE-SWCNT-NiO.

The EDX profile (Figure 4.3) of the modified electrodes showed well-defined nickel peaks, confirming the successful electrodecoration of the EPPGE-confined SWCNTs. The acid-treated SWCNT (b) showed traces of nickel impurities. The pronounced

sulphur peak could have arisen from the sulphuric acid solution used in the functionalization and washing processes in agreement with the FTIR data. The occurrence of P and Na peaks in the EDX of EPPGESWCNT-NiO (b) is associated with the treatment of the electrode with sodium phosphate buffer solution while the enhanced oxygen peak also confirms the modification of the electrode to its oxide form.

4.2 Comparative redox chemistry in aqueous solution

Figure 4.4 shows examples of voltammetric responses of the electrodes, EPPGE, EPPGE-NiO, EPPGE-SWCNT and EPPGE-SWCNT-NiO, indicating successful integration of the nickel particles with the SWCNTs, confirmed by features such as (i) the presence of the well-defined redox waves of the surface-confined Ni(II)/Ni(III) ($E_{1/2}$ ≈ 0.45V vs. Ag|AgCl, sat'd KCl); (ii) the increased current response following the incorporation of the nickel with the SWCNTs, and (iii) the high charge (capacity) of the EPPGE-SWCNT-NiO compared to other electrodes. EPPGE-SWCNT also exhibited a pair of weak redox peak (E_a ≈ −0.02V and E_c ≈ −0.30 V), which is typical of immobilized SWCNTs at a carbon electrode [5]. The two pairs of redox processes shown by the EPPGE-SWCNT-NiO (E_a ≈ −0.03 V (I) and E_c ≈ −0.44 V (I^I)) and (E_a ≈ 0.67 V (II) and E_c ≈ 0.20V (II^I)) are attributed to the redox processes of the surface-confined SWCNTs and Ni(II)/Ni(III), respectively. An interesting observation here is the significant decrease in the peak-to-peak separation potential (ΔE_p) value of the Ni(II)/Ni(III) redox process in the presence of SWCNTs (ΔE = 0.47 V) compared to the absence of SWCNTs ΔE_p = 0.70 V), indicating a faster electron transport due to the SWCNTs.

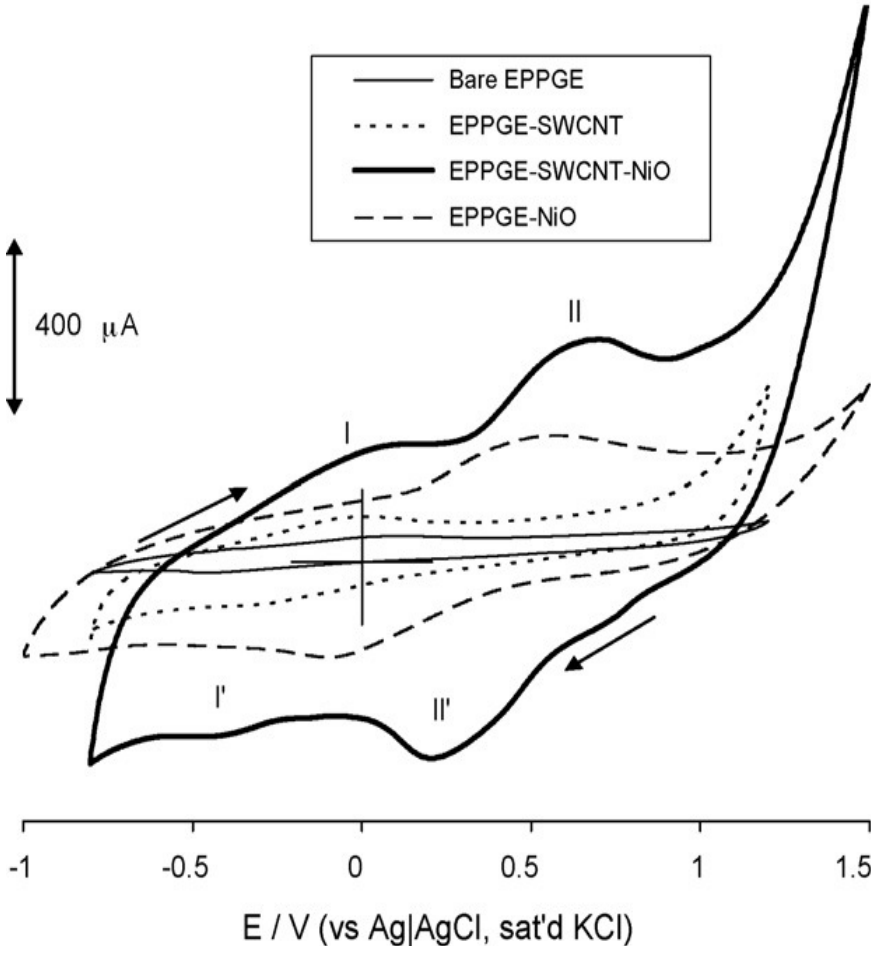

Figure 4.4: Comparative current response of the bare-EPPGE, EPPGE-SWCNT, EPPGE-NiO and EPPGE-SWCNT-NiO in pH 7.0 PBS. Scan rate = 50m Vs^{-1}.

Electrodes modified with nickel hydroxide films are well reported for electrocatalysis and sensing applications. Figure 4.5a shows an example of voltammetric evolutions obtained during continuous scanning (20 scans) of the EPPGE-SWCNT-Ni (obtained at 5 min potentiostatic deposition time) in 0.1M NaOH to form the EPPGE-SWCNT-$Ni(OH)_2$. The first scan appeared with two broad anodic peaks (E_{pa}) at around 0.12 V and 0.73 V with a sharp return cathodic peak at 0.36 V.

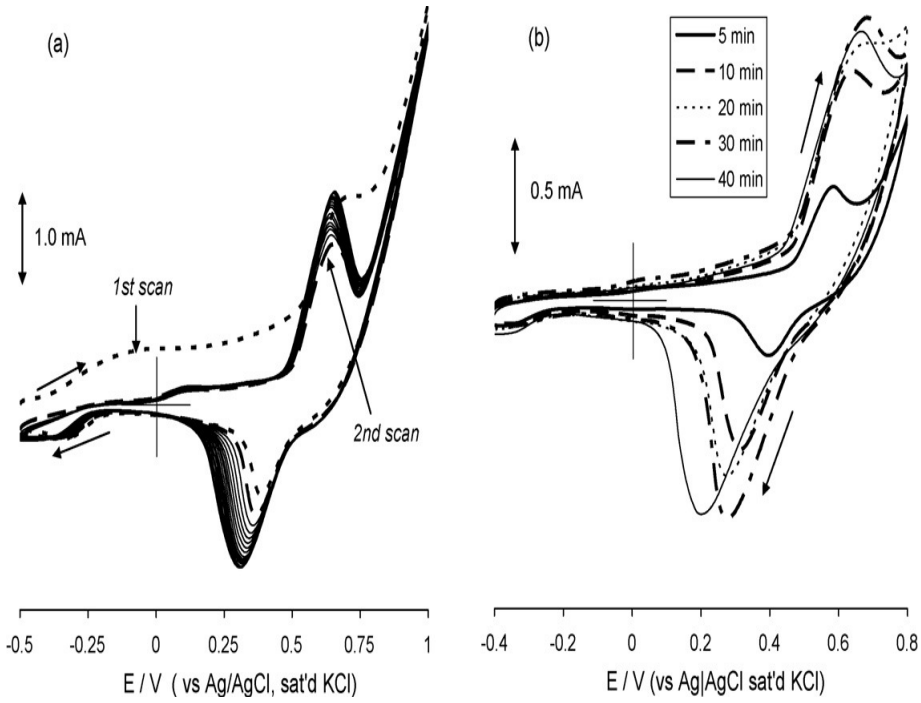

Figure 4.5: (a) Repetitive cyclic voltammetric evolution (20 scans) of EPPGE-SWCNT-Ni in 0.1M NaOH solution. (b) Comparative cyclic voltammetric evolution (1st scan) of the EPPGE-SWCNT-Ni in 0.1M NaOH at different nickel deposition time (5–40 min). Scan rate = 100 mVs^{-1}.

In accordance with literature [6–8], the first anodic peak of this first scan may be ascribed to the oxidation of the Ni(0) to the α-$Ni(OH)_2$ (Equation 4.1), while the anodic peak at the higher potential is due to the conversion of the α-$Ni(OH)_2$ to its β-$Ni(OH)_2$ form (Equation 4.2):

$$Ni + 2OH^- \longrightarrow \alpha\text{-}Ni(OH)_2 + 2e^- \quad (4.1)$$

$$\alpha\text{-}Ni(OH)_2 \longrightarrow \beta\text{-}Ni(OH)_2 \quad (4.2)$$

The weak cathodic peak observed at −0.36 V is attributed to the reduction of unconverted α-$Ni(OH)_2$ to Ni. Salimi et al. [8] indicated they observed such peak at −0.30 V with their nickel powder-doped

carbon composite electrode. The second scan occurred with a sharp peak at E_{pa} = 0.66 V with a decrease in the anodic current (*ca.* 500 μA) compared to that of the first scan, suggesting that β-$Ni(OH)_2$ has been formed on the electrode surface, poisoned it. During this second scan, the β-$Ni(OH)_2$ is first oxidized via proton coupled reaction to the β-NiOOH (and possibly to a very small amount of γ-NiOOH, assume <1% [7]) (Equation 4.3), which is subsequently reduced to the β-$Ni(OH)_2$ species (Equation 4.4).

$$\beta\text{-}Ni(OH)_2 + OH^- \longrightarrow (\beta,\gamma)\text{-}NiOOH + H_2O + e^- \quad (4.3)$$

$$(\beta,\gamma)\text{-}NiOOH + H_2O + e^- \longrightarrow \beta\text{-}Ni(OH)_2 + OH^- \quad (4.4)$$

It should be noted that during the second cycle the peak at 0.12V was no longer observed. According to the interpretation made by a similar observation by Czerwinski and co-workers [6,7], such behaviour of nickel electrode is not unusual and is associated with the inability of the β-$Ni(OH)_2$ formed from the fresh α-$Ni(OH)_2$ in Equation (4.2) to be transformed back to the α-$Ni(OH)_2$. This irreversible transition process is described as the "aging effect" [7]. It is noteworthy that several reports [6-8] acknowledge that *α*-$Ni(OH)_2$ transforms to the *β*-$Ni(OH)_2$ slowly during the potential scans and accumulate on the electrode surface. The results therefore imply that the conversion of the *α*-$Ni(OH)_2$ to the *β*-$Ni(OH)_2$ on the EPPGE-SWCNT surface occurs much faster than on bulk electrode surfaces. The shift of the cathodic peak from about 0.37 V at the onset of the electrochemical process to ≈ 0.30 V at the 20^{th} scan is attributed to the difficulty of reducing the *β*-NiOOH to *β*-$Ni(OH)_2$ as the scan number increases.

To gain some insights into the impact of electrodeposition time of nickel nanoparticles on electron transport in alkaline conditions, the cyclic voltammetric evolutions obtained at different deposition time of nickel nanoparticles on the EPPGE-SWCNT surface was compared. The impact of deposition time was examined because many literature reports on electrodes electrodeposited with metal particles have used deposition time (usually in the ≤5min) but did not provide reasons for such choices. Figure 4.5b compares cyclic voltammograms (using first scans) obtained for the EPPGE-SWCNT-Ni in 0.1 M NaOH at different electrodeposition time (5 – 40 min) of the nickel nanoparticles onto the EPPGE-SWCNT surface. The voltammetric peak heights increased simultaneously with deposition time, stabilizing at 30 min. Also, the surface concentrations of the nickel nanoparticles increased from about 10 nmol cm^{-2} at 5 min to 57 nmol cm^{-2} at 40 min. The ΔE increased from 0.28 V at 5 min to 0.47 V at 40 min. The stabilisation of both the anodic and cathodic peak current heights at 30 min and the increased ΔE values are indicative of some kinetic frustrations possibly due to the increased generation of the inactive β-NiOH from the α-$Ni(OH)_2$ species as more nickel nanoparticles are deposited on the electrode surface. This interpretation is in agreement with previous reports which suggest that α-$Ni(OH)_2$ slowly and steadily transforms to β-NiOH species [6-8].

Preliminary investigation on the impact of scan rate on the EPPGE-SWCNT-Ni in 0.1M NaOH (Figure 4.6) was only possible between 25 and 300mVs^{-1} as very high peak-to-peak separation (ΔEp) values, ranging from 0.5 V at 25 mVs^{-1} to 1.6 V at 300 mVs^{-1} were obtained. This result means that, in this electrolyte conditions, as the scan rate is increased the electrode reactions become irreversible, typical of poor electron transport behaviour. This also reflects a slow diffusion of hydroxide ions into the limited

wetting section of electrode surfaces [8]. It was observed that the ratio of cathodic to anodic peak currents is less than unity, suggesting possible side reactions. Thus, no further investigation on the effect of scan rate was carried out in this initial report. However, it should be stated that in future investigations on the possible applications of this electrode in the alkaline conditions (such as in electrocatalysis and sensing of organic species) more detailed electrochemical studies should be performed on these deposition time especially to establish, for example, the possible impact of deposition time on the electrocatalytic response of the analytes at the different deposition time and scan rates.

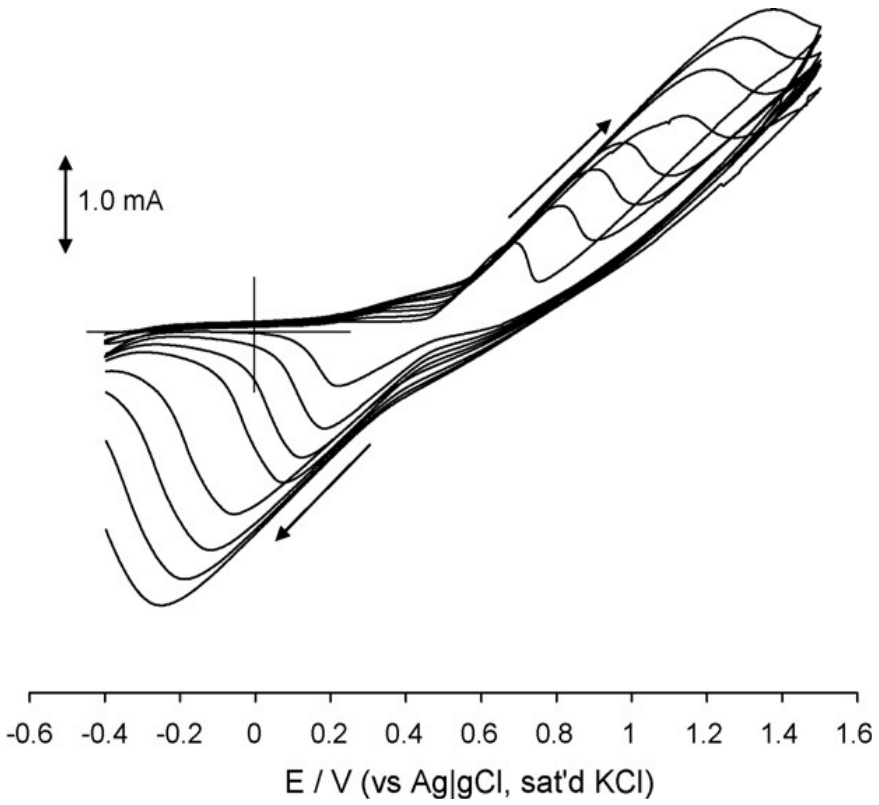

Figure 4.6: Voltammetric evolutions of EPPGE-SWCNT-Ni in 0.1MNaOHsolution at varying scan rates of 25, 50, 75, 100, 150, 200, 250 and 300 mVs^{-1} (inner to outer). The electrode was obtained at 5 min deposition and used for the study after 2nd scan.

4.3 Comparative Electron Transport Properties

The electron transport features of the various Ni and NiO modified electrodes were interrogated using 0.1 M pH 7.0 PBS containing 5 mM $[Fe(CN)_6]^{4-}$ / $[Fe(CN)_6]^{3-}$ as redox probe (Figure 4.7). Some interesting observations are made from the comparative CVs. First, the Faradaic current responses follow the trend: EPPGE-SWCNT-Ni > EPPGE-SWCNT >> EPPGE-Ni > EPPGE-SWCNT-NiO > EPPGE-SWCNT-$Ni(OH)_2$ > EPPGE-NiO > EPPGE-Bare > nickel disk > nickel disk hydroxide.

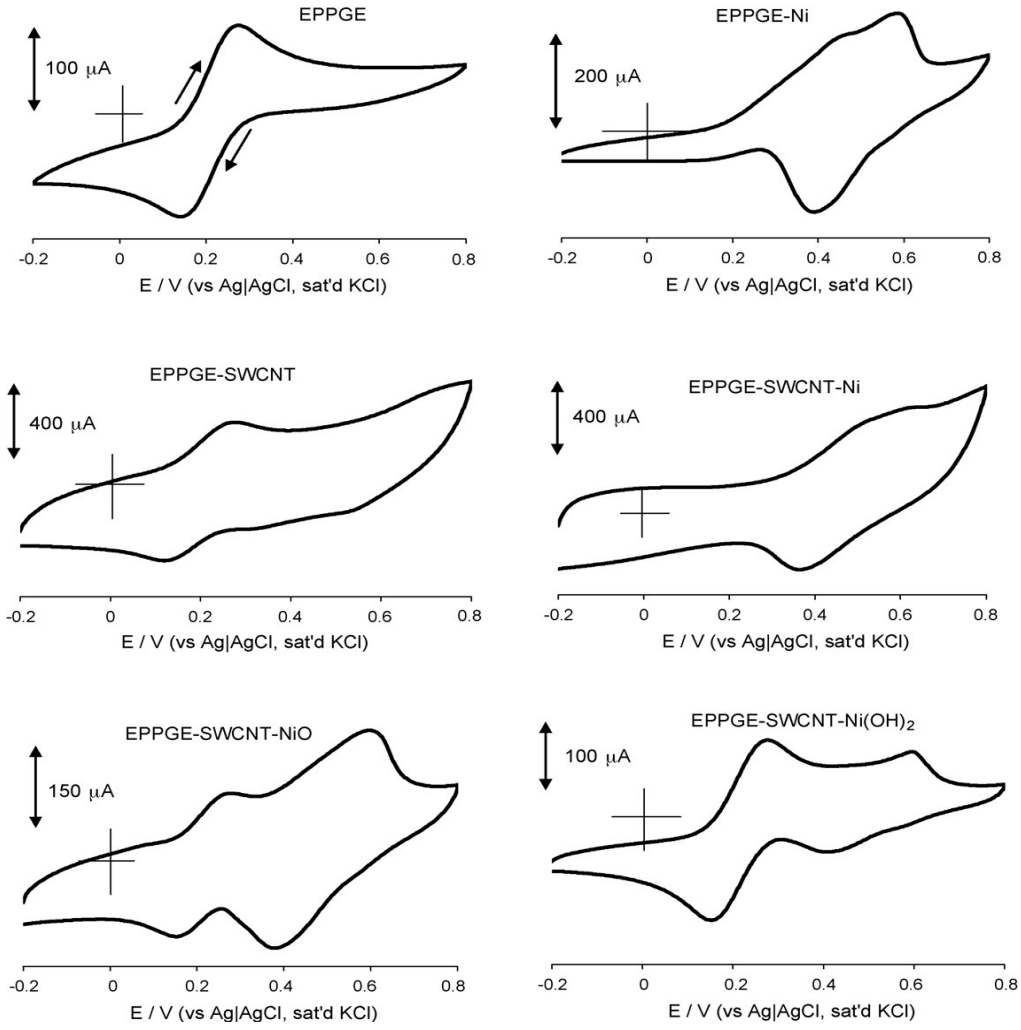

Figure 4.7: Typical examples of cyclic voltammetric evolutions of the electrodes in 5mM $[Fe(CN)_6]^{4-}/[Fe(CN)_6]^{3-}$ solution (PBS pH 7.0). Scan rate = 50 mVs^{-1}.

All the electrodes coated with nickel nanoparticles gave two redox processes occurring in the +0.0 to 0.4 V and +0.4 to 0.55 V regions, which was assigned to the $[Fe(CN)_6]^{4-}/[Fe(CN)_6]^{3-}$ and Ni(II)/Ni(III) redox processes, respectively. Second, all the electrodes coated with nickel nanoparticles, prior to passivation with the oxide layer, showed broad peaks with higher current response compared to others without nickel nanoparticles. These broad peaks (see for example, the EPPGE-SWCNT-Ni) were attributed to the overlap of the $[Fe(CN)_6]^{4-}/[Fe(CN)_6]^{3-}$ and Ni(II)/Ni(III) redox processes. The passivation with the oxide layer resulted in the separation of these two overlapped peaks. Upon electrochemical decoration of the EPPGE-SWCNT surface with nickel nanoparticles, an increased current response of the EPPGE-SWCNT-Ni compared to other electrodes was observed. This results suggests that the two modifiers (SWCNTs and nickel films) synergistically mediate the one-electron transport of the $Fe(CN)_6]^{4-}/[Fe(CN)_6]^{3-}$ across the EPPGE-SWCNT-Ni|solution interface.

For further insights into the electron transport properties of the electrodes, an electrochemical impedance spectroscopy (EIS) experiments at potential corresponding to the $E_{1/2}$ of the $[Fe(CN)_6]^{4-}/[Fe(CN)_6]^{3}$) were carried out. Figure 4.8 shows the experimental and the fitted Nyquist plots obtained. Every attempt to fit the EIS data with the original Randles model [9] which refers to the 'true' Faradaic process (i.e., true charge transfer at the metal|electrolyte interface but not to the partial charge transfer process) proved unsuccessful. However, using the equivalent circuit models incorporating the constant phase element (CPE, Figure 4.9) yielded remarkable improvements as evident from the acceptable percentage error values in Table 4.1. Note that it is from the fitted solid lines in Figure 4.8 that the R_s (the solution/electrolyte

resistance), R_{ct} (charge transfer resistance), and Z_w (Warburg impedance) related to the semi-infinite linear diffusion were obtained.

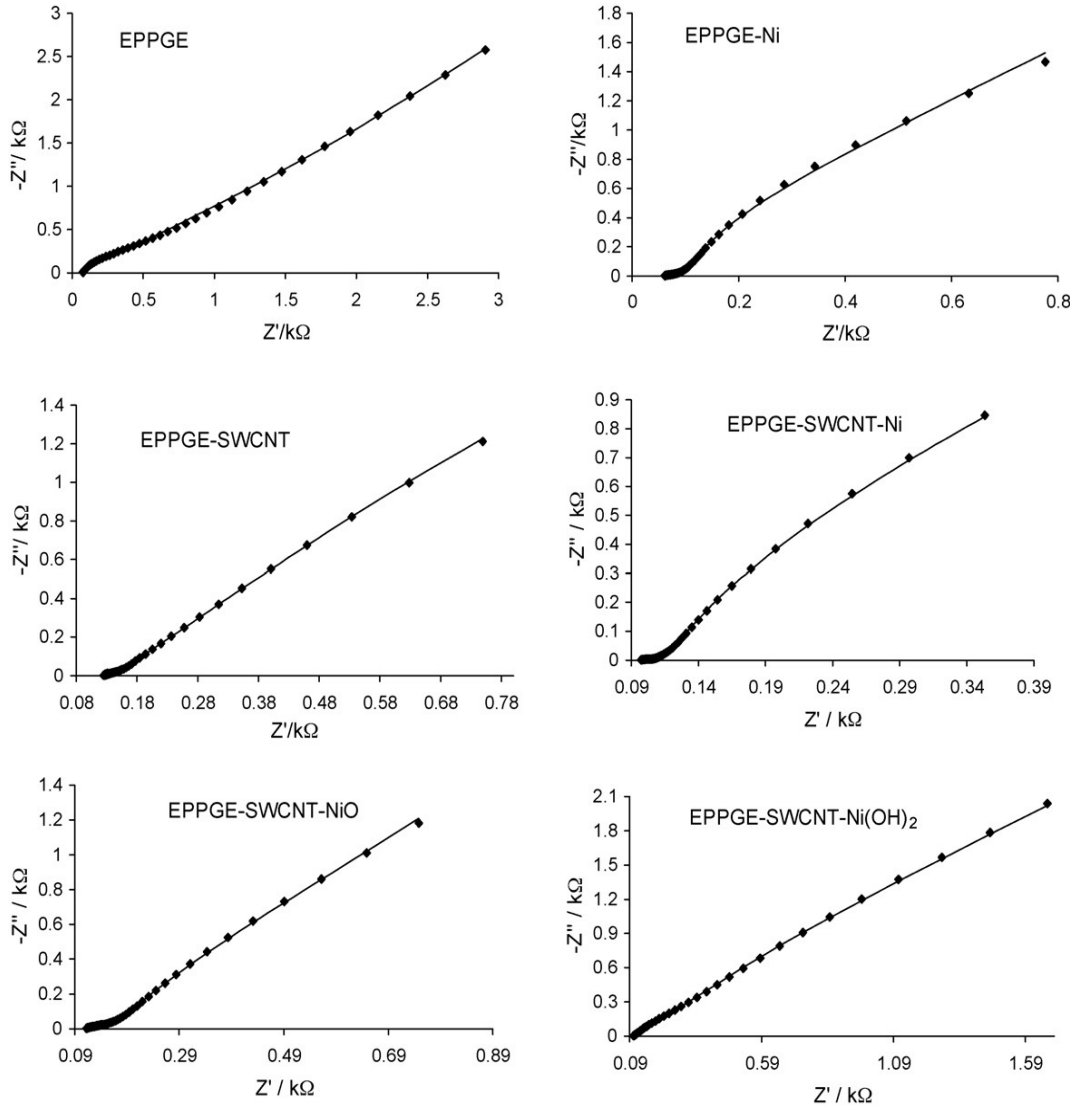

Figure 4.8: Typical Nyquist plots of the of the electrodes obtained in 5mM $[Fe(CN)_6]^{4-}/[Fe(CN)_6]^{3-}$ solution (PBS pH 7.0) at fixed potential of 0.30 V vs. Ag|AgCl sat'd KCl.

In Figure 4.9, equivalent circuit (a) was used to fit the bare EPPGE, EPPGE-SWCNT and nickel disk hydroxide electrodes, the equivalent circuit (b) was used to fit the EPPGE-Ni, EPPGE-SWCNT-Ni, EPPGE-SWCNT-NiO and EPPGE-NiO, while EPPGE-SWCNT-$Ni(OH)_2$ was best fitted with equivalent circuit (c). These results

have certain implications. First, in the absence of nickel nanoparticles, the electrodes essentially follow the Randles equivalent circuit, except that the capacitor of the electric double layer (C_{dl}) deviated from a pure capacitor because of the roughness of the electrode and so is replaced by a CPE (Figure 4.9a) [9-13]. Second, in the presence of nickel films, the structure of the electrode interface is altered leading to different models (circuits 4.9b and 4.9c). Several literature reports [9-13], associate parallel connection of R_{ct} with impedance as some electrode processes involving electrochemically adsorbed products, thus the R_{ct} here may be associated with adsorption or partial charge transfer resistance of the nickel and nickel oxide films. Also, equivalent circuits 4.9b and 4.9c exhibit good resemblance to the circuit of the so-called "electrolyte-insulator-semiconductor (EIS)" sensors [14]. An electrolyte-insulator-semiconductor device comprises a doped semiconductor acting as substrate for a thin insulating layer, normally an oxide or nitride, which can be immersed in an electrolyte containing a fixed concentration of anionic species to be measured [14]. The CPE_1 is ascribed to the energetic inhomogeneity arising from the surface roughness of the electrode ($n \approx 0.73$). The CPE_2 observed for the EPPGE-SWCNT-$Ni(OH)_2$ may be associated with the inhomogeneous semi-infinite diffusion of the probe to the electrode surface since the value of $n \approx 0.52$ indicates small deviation from the ideal semi-infinite diffusion model ($n = 0.5$) to mixed (diffusion and adsorption ($n = 1.0$) limited) kinetics. At the experimental conditions employed here, the EIS data (Table 4.1) indicate that EPPGE-SWCNT-Ni gave the least resistance to electron transfer, approximately 30 times smaller than the EPPGE-SWCNT-NiO, 25 times smaller than EPPGE-SWCNT, and between 300 and 9000 times smaller than the bare EPPGE, EPPGE-SWCNT-$Ni(OH)_2$), and nickel disk.

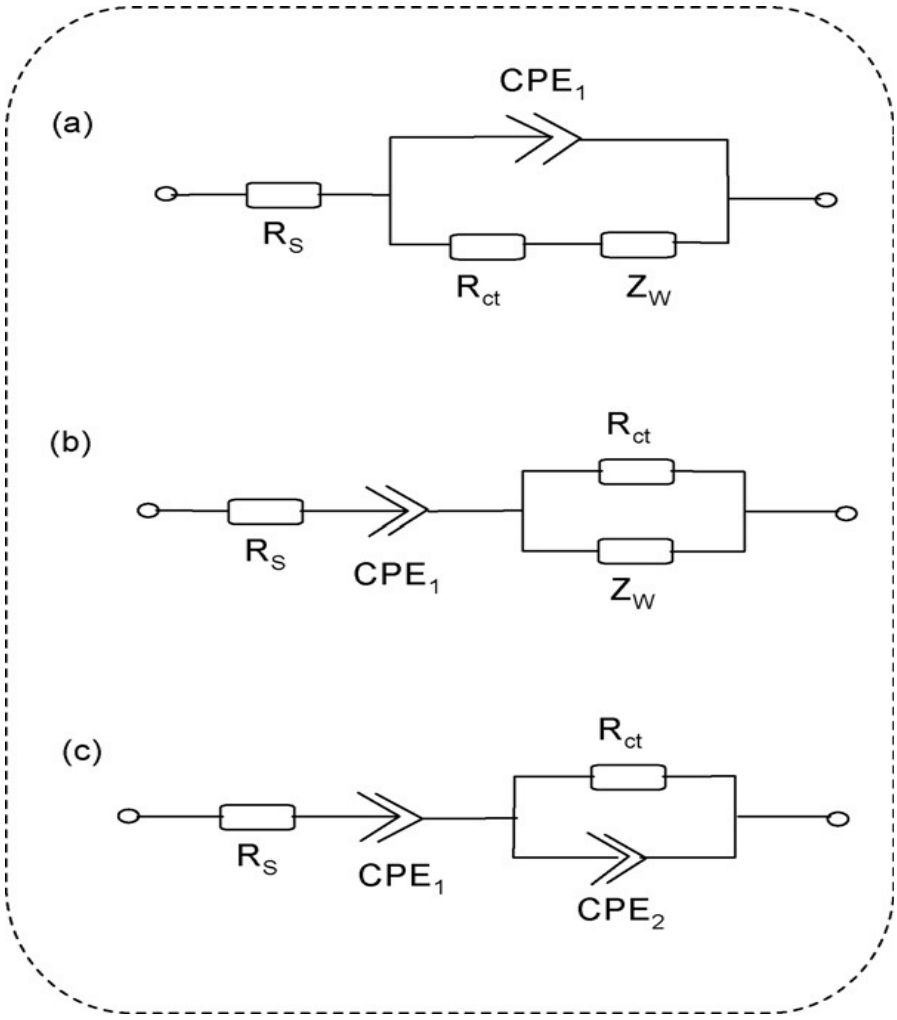

Figure 4.9: Equivalent circuit diagrams used for fitting the impedance data obtained in this work. Circuit (a) was used to fit the bare EPPGE, EPPGE-SWCNT and nickel disk hydroxide electrodes; (b) was used to fit the EPPGE-Ni, EPPGE-SWCNT-Ni, EPPGESWCNT-NiO and EPPGE-NiO; (c) was used for EPPGE-SWCNT-Ni$(OH)_2$.

It is well established that the formation of the passive oxide layer on surface-confined nickel nanoparticles impede electron transport [15]. This behaviour may be interpreted as the result of increased electrical resistance and the resistance to mass transport through the film as the film thickness increases [16]. Thus, it may be concluded here that the high current response of the EPPGE-SWCNT-Ni is the combination of two factors; the inherent faster electron transfer of the nickel nanoparticles (i.e., large surface area)

and the overlap of the $[Fe(CN)_6]^{4-}/[Fe(CN)_6]^{3-}$ and Ni(II)/Ni(III) redox processes. It is not surprising that bulk nickel metal disc electrodes, modified or unmodified, gave the least Faradaic response in this redox probe system compared to their nanoparticle-based electrodes. The n values extracted from the equivalent circuit were approximately in the 0.5 – 0.9 range, suggesting that the electrodes generally exhibit pseudocapacitive behaviour.

To obtain more useful information on the electrical properties of the films, Bode plots were compared (exemplified in Figure 4.10). From Figure 4.10a (–phase angle vs log f), the Ni disk $(OH)_2$ showed one symmetric peak, which corresponds to the relaxation process of the electrode|solution interface. The appearance of this peak at wide potential range is indicative of complex and irregular surface properties of this bulk electrode. From the other type of Bode plot (log |Z| on log f, Figure 4.10b), the electrodes yielded slopes in the –0.40 to –0.60 range, confirming the presence of a CPE. The higher phase angles of the nickel nanoparticles (–67^o at 0.13 Hz for EPPGE-SWCNT-Ni and –65^o at 0.2 Hz for the EPPGE-Ni) compared to their solution treated counterparts (–58^o at 0.1 Hz for EPPGE-SWCNT-NiO, –46^o at 0.16 Hz for the EPPGE-NiO and –51^o at 0.2 Hz for EPPGE-SWCNT-$Ni(OH)_2$) may be interpreted in terms of the nickel nanoparticles exhibiting more capacitive behaviour (better structural organisation) than when treated in buffer or alkaline solutions since ideal capacitive systems should give phase angles of *ca.* –90^o.

Table 4.1: Impedance data obtained for the modified electrodes in 5 mM $[Fe(CN)_6]^{4-}/[Fe(CN)_6]^{3-}$ solution (PBS pH 7.0) at 0.30 V vs. Ag|AgCl sat'd KCl. All values were obtained from the fitted impedance spectra after several iterations using the circuits. Note that the values in parentheses are errors of data fitting.

ELECTRODES	**Electrochemical Impedance Parameters**						
	R_s / Ω cm^2	**CPE_1/ mFcm^{-2}**	**n**	**10^5 Z_W/ Ω cm^2**	**R_{ct} / Ω cm^2**	**CPE_2 / mFcm^{-2}**	**10^3K^0 Cms^{-1}**
EPPGE	8.86±0.06	0.30±0.02	0.78	3.97±0.03	58.20±2.10	-	0.91
EPPGE-SWCNT	12.43±0.06	1.00±0.01	0.73	19.07±1.81	2.48±0.15	-	21.46
EPPGE-SWCNT-Ni	5.26±0.05	17.30±0.09	0.86	6.99±0.57	0.11±0.05	-	483.72
EPPGE-SWCNT-NiO	6.37±0.05	107.60±0.65	0.74	5.17±0.39	3.28±0.15	-	16.22
EPPGE-Ni	1.40±0.03	9.10±0.12	0.81	2.62±0.23	0.75±0.06	-	70.95
EPPGE-NiO	6.74±0.49	4.70±0.06	0.57	2.50±0.23	1.58±0.16	-	33.68
EPPGE-SWCNT-Ni(OH)$_2$	11.15±0.03	2.70±0.22	0.73	-	44.29±4.30	2.80±0.27	1.20
NICKEL DISK	1.82±0.10	0.10±0.01	0.64	0.04±0.01	922.35±80.25	-	0.06
NICKEL DISK(OH)$_2$	2.17±0.01	0.10±0.00	0.82	0.17±0.00	325.73±2.61	-	0.16

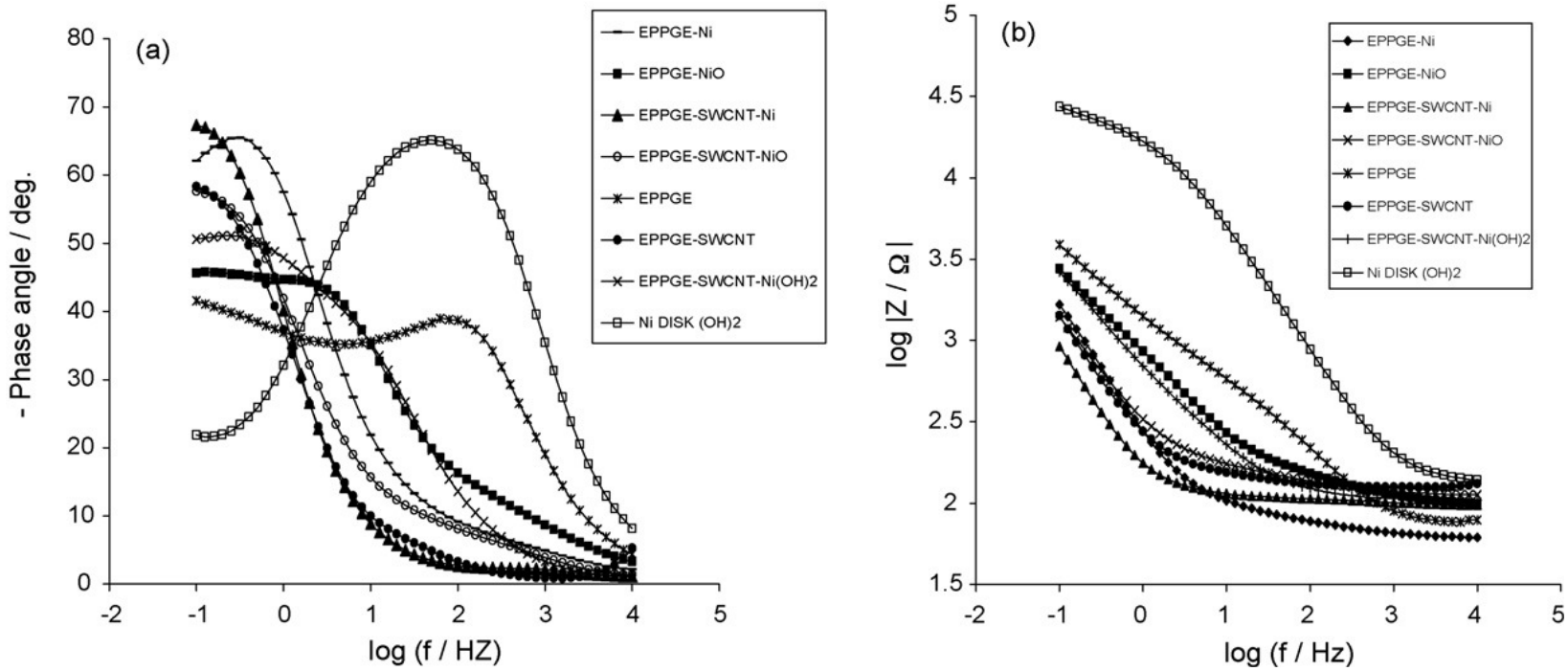

Figure 4.10: Bode plots obtained for the electrodes obtained at 0.30V vs. Ag|AgCl sat'd KCl.

4.4. Electrochemical response of the Ni-modified electrodes towards DEAET oxidation.

Figure 4.11 compares the electrocatalytic response of the various electrodes toward the oxidation of DEAET in pH 9.4 PBS, clearly showing better response of EPPGE-SWCNT-Ni (in terms of onset potential and peak current) over the other electrodes EPPGE, EPPGE-SWCNT, EPPGE-Ni, EPPGE-NiO and EPPGE-SWCNT-NiO. The EPPGE-SWCNT-Ni showed onset potential at about 0.4 V compared to others which appeared around 0.5 V. The broad voltammogram shown by the EPPGE-SWCNT-Ni may be attributed to its porous nature and the high electroactive surface area compared to other electrodes. These properties were lost on the treatment of the EPPGE-SWCNT-Ni in pH 7.0 PBS for the formation of the EPPGE-SWCNT-NiO electrode. The surface transformation between the Ni and the NiO nanoparticles modified electrodes are clearly described by their AFM and SEM images (Figure 4.2). However, background-subtracted voltammogram (not shown) clearly showed the reversible couple with formal potential ($E_{1/2}$) around 0.0 V, which was ascribed to the Ni(II)/Ni(III) redox couple that mediate this enhanced electrocatalytic activity toward DEAET. In all, the EPGGE-SWCNT-Ni gave better response towards DEAET, hence all subsequent studies were carried out with this electrode.

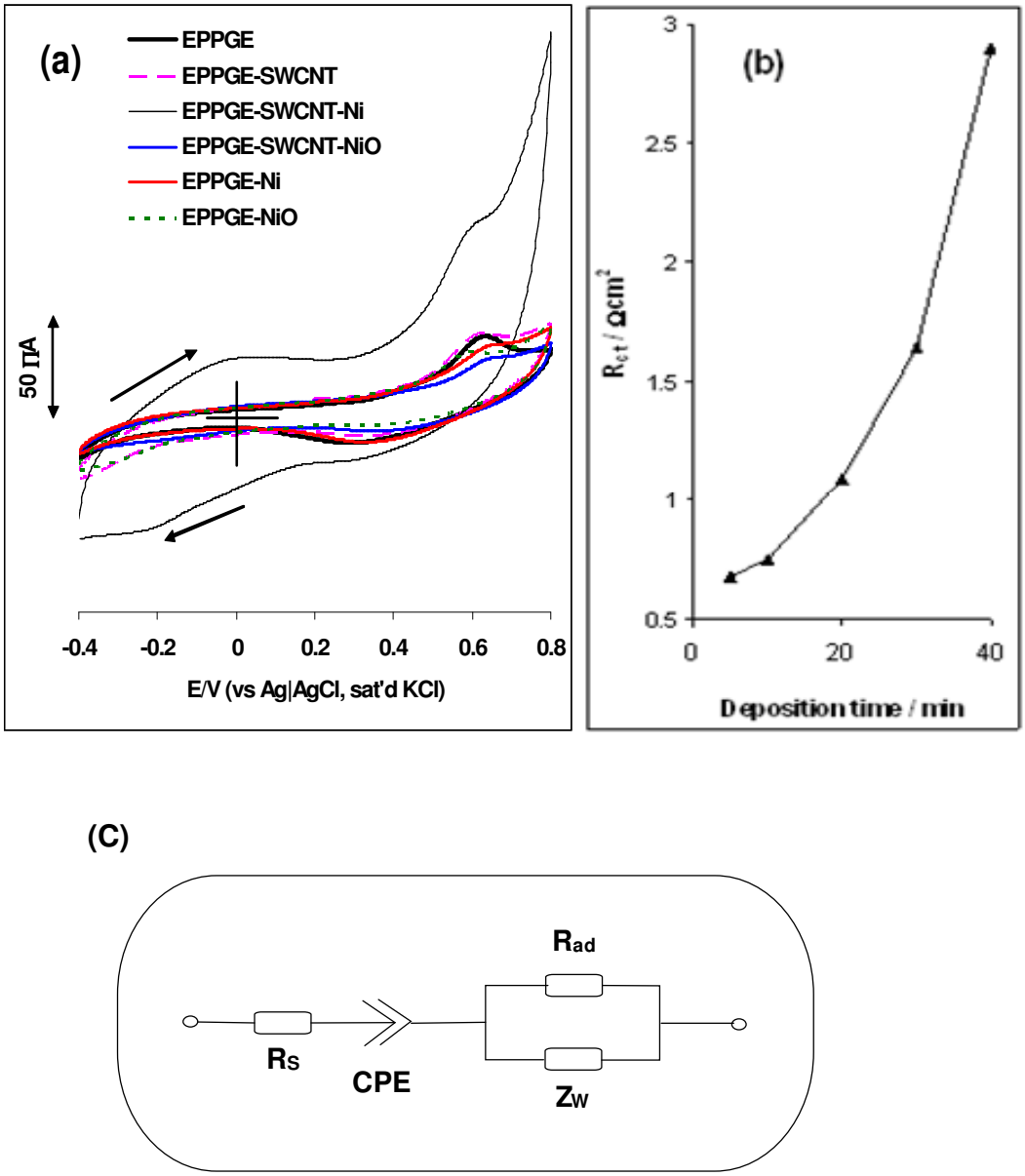

Figure 4.11: (a) Examples of comparative cyclic voltammograms recorded at the various electrodes in 0.1 M PBS (pH 9.4) containing 0.1 mM DEAET. (b) Plot of charge transfer resistance (R_{ct}) against deposition time of nickel (biased at 0.6 V vs Ag|AgCl, sat'd KCl) obtained at EPPGE-SWCNT-Ni. (c) Circuit diagram used in the fitting of impedance data in (b).

4.5 Comparative electrochemical response to DEAET at different Ni deposition time

Next, the impact of nickel deposition time (using same concentration of the nickel salt) on the current response of the DEAET at EPPGE-SWCNT-Ni was studied. Figure 4.11b shows examples of impedance spectra obtained at EPPGE-SWCNT-Ni in 0.1 M PBS (pH 9.43) containing 10^{-4} M DEAET at different electrodeposition time of the nickel nanoparticles (bias potential = 0.6 V vs Ag|AgCl, sat'd KCl). From the plot of charge transfer resistance against deposition time, it is clearly seen that the best current response was at 5 min deposition time. The same behaviour was observed with CV experiments (not shown) where 5 min deposition exhibited the best current response. The decreased current response or charge transport at > 5 min was attributed to the formation of the β-NiOH species well known to hinder the nickel reactivity [17].

The electrical circuit compatible with the impedance spectra is shown in Figure 4.11c. The R_{ct} was nicely fitted using electrical circuit wherein the R_s and Q (or CPE) are in series connected to the R_{ct} and Z_w which are in parallel, compatible with the impedance spectra (not shown) which incorporates R_s (the solution/electrolyte resistance), R_{ad} (partial charge-transfer or adsorption resistance), Z_w (Warburg impedance) related to the semiinfinite linear diffusion, and CPE (constant phase element). It is noteworthy that the equivalent electrical circuit $R_sQ(R_{ct}Z_w)$ used in fitting the impedance spectra for Figure 6.11b suggests that the oxidation of DEAET at the EPPGE-SWCNT-Ni is proceeded by a mechanism that includes adsorption. Parallel connection of R_{ad} with impedance is indicative of electrode processes involving electrochemically adsorbed products or intermediates [18].

Mechanisms that include adsorption step, in many instances, lead to passivation of the active surface of the electrode. CV experiment of the electrode at constant concentration of the DEAET showed same decrease in the peak current after the first scan, which is characteristic of electrode passivation. However, on rinsing the electrode in a buffer solution (pH 9.4) and repeating the experiment in DEAET solution, about 80% of the original current was observed suggesting partial recovery of the electrode. Similarly, after keeping the electrode for a period of four weeks and its catalysis towards DEAET oxidation was investigated, an oxidation current, very close to the same current generated four weeks earlier for the same concentration of DEAET was observed. This result suggests that the Ni nanoparticles decorated on the SWCNTs have a long-term stability that could be employed in sensing applications.

4.6 Electroanalysis of DEAET

4.6.1 Scan rate study

Cyclic voltammetry at varying scan rates (0.02 to 0.5 Vs^{-1}) of the EPPGE-SWCNT-Ni in 10^{-4} M DEAET solution showed poor linear relationship between the plot of the oxidative peak current (I_p) against the square root of scan rate ($\nu^{1/2}$) (R^2 = 0.9843) while at scan rates > 0.3 Vs^{-1}, the oxidative peak current became broad making it difficult to measure. The scan rate results show that the oxidation of DEAET species in the solution is adsorption-controlled process. For irreversible reactions [19], the peak potentials should vary with the log of the scan rates according to:

$$E_p = \frac{b}{2}\log \nu + const. \qquad (4.5)$$

All symbols retain their usual meanings. On the basis of the δEp/δlogv slopes of the plots of E_p vs log ν, the value of the Tafel slope was estimated to be *ca.* 260.0 $mVdec^{-1}$, indicating that the rate-determining step for the catalysis involves a one-electron transfer process. According to literature [20], high Tafel slopes (> 120 $mVdec^{-1}$) for a one-electron process) as obtained in this study is the consequence of strong binding of reactants or intermediates on the electrode surfaces and/or reactions occurring within a porous electrode structure. Thus, the Tafel slopes obtained in this work can be attributed to the adsorption of DEAET on the electrode.

4.6.2 Comparative Electrocatalytic Response: Adsorption Stripping Voltammetric and Chronoamperometry.

Two sensitive electrochemical methods, adsorptive stripping voltammetry and chronoamperometry, were used to investigate the impact of varying concentrations of DEAET to current response at the EPPGE-SWCNT-Ni platform. The former method was used for high concentration range (0.0, 28.6, 33.3, 37.5, 41.2 and 44.5 μM (i to vi)), Figure 4.12a) while the later technique was employed for low concentration range (0.0, 20, 40, 60, 80, 100 nM (i to vi), Figure 4.12b). To reduce the effect of adsorption during the chronoamperometric experiments, the electrode surface was conditioned between measurements by rinsing in buffer solution (pH 9.4).

The values of the limit of detection (LoD = 3.3 δ/m, where *δ* is the relative standard deviation of the intercept of the y-coordinates from the line of best fit, and *m* the slope of the same line) and limit of

quantification (LoQ = 10 δ/m) are summarized in Table 4.2. The quantification limit describes the lowest concentration of an analyte that can be quantified with acceptable precision and accuracy. When compared to the presently available literature reports on the electrocatalytic detection of DEAET (Table 4.2), it is easily observed that results obtained by these two techniques are comparable and even better than data obtained to date for the detection of DEAET.

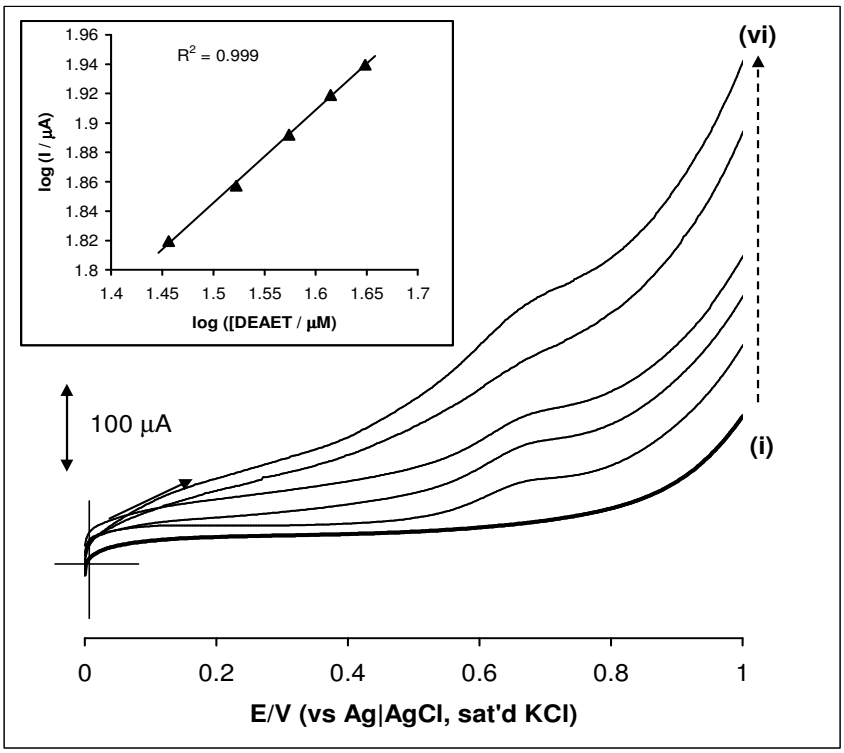

Figure 4.12: (a) Typical examples of linear sweep voltammetric evolutions of EPPGE-SWCNT-Ni in phosphate buffer solution (pH 9.4) containing different concentrations of DEAET (0.0, 28.6, 33.3, 37.5, 41.2 and 44.5 µM (i to vi)). Inset is plot of log current response (background-subtracted) vs log DEAET concentrations.

Also the electrode platform gives some notable advantages over other reports such as the avoidance of the use of enzyme [21], or cocktails of redox-active electropolymers [22], or the employment of

derivatization reactions between thiols and *o*-phthaldialdehyde [23,24]. The enhanced sensitivity obtained in this report may be ascribed to the ability of the SWCNTs to function as efficient conducting species for the catalytic nickel nanoparticles.

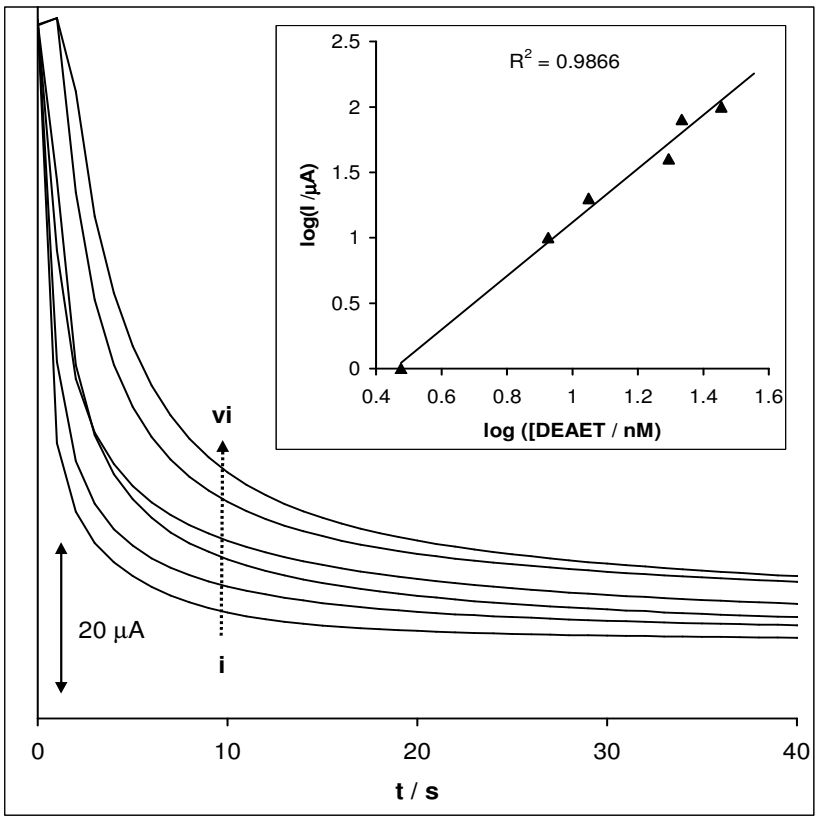

Figure 4.12: (b) Typical examples of chronoamprometric evolutions of EPPGE-SWCNT-Ni in phosphate buffer solution (pH 9.4) containing different concentrations of DEAET (0.0, 20, 40, 60, 80 100 nM (i to vi)) at fixed potential 0.6V vs Ag|AgCl, sat'd KCl. Inset is plot of log current response (background-subtracted) vs log DEAET concentrations.

Table 4.2: Comparative analytical data for the detection of DEAET at chemically modified electrodes

Electrode	**Analytical Parameter**[a]					
	Sensitivity	**LoD**	**LoQ**	ΔG^o	β	**Ref**
SPE- MWCNT-OPH	0.036 µA/mM	8.0 µM	-	-	-	21
GCE-PPy-PQQ	1.37 nA/µMcm^2	3.0 µM	-	-	-	22
BPPGE-SWCNT-CoTAPc	0.06 A/M	3.0 µM	-	-	-	25
BPPGE-Ni powder	0.023 A/M	4.0 µM	-	-	-	26
EPPGE-SWCNT-Ni[b]	1.29±0.10 A/M	2.5 ±0.23 µM	7.6±0.65 µM	–24.80 kJ mol^{-1}	2.2 x 10^4 M^{-1}	This work
EPPGE-SWCNT-Ni[c]	0.18±0.01 µA/nM	5.2±0.42 nM	15.7±1.3 nM	– 45.8 kJ mol^{-1}	10.6x10^7 M^{-1}	This work

[a]All reference electrodes were reported against Ag|AgCl wire with the exception of this present work and GCE-PPy-PQQ which were reported against Ag|AgCl (3M KCl); Screen-printed carbon electrode modified with multi-walled carbon nanotubes and organophosphorus hydrolase; Glassy carbon electrode modified with poplypyrrole and pyrroloquinoline quionone. Basal plane pyrolytic graphite electrode modified with single-walled carbon nanotube and cobalt tetraaminophthalocyanine; Basal plane pyrolytic graphite electrode modified with nickel micropowders (of size distributions in the ~17 - 60 µm range). [b]Obtained by adsorption stripping voltammetry. [c]Obtained by chronoamperometry.

Based on the results obtained here and previous reports on the mechanism of thiol electro-oxidation at modified electrodes [27], the following mechanism was proposed:

$$RSH + OH^- \rightleftharpoons RS^- + H_2O \quad (4.6)$$

$$RS^- + [SWCNT\text{-}Ni^{2+}]_{film} \rightleftharpoons [SWCNT\text{-}Ni\text{---}(SR)]^{2+}_{film} \quad (4.7)$$

$$[SWCNT\text{-}Ni\text{---}(SR)]^{2+}_{film} \longrightarrow [SWCNT\text{-}Ni^{3+}]_{film} + RS^{\bullet} + e^- \ (slow) \quad (4.8)$$

$$RS^{\bullet} + RS^{\bullet} \longrightarrow RSSR \ (fast) \quad (4.9)$$

$$[SWCNT\text{-}Ni^{3+}]_{film} + e^- \longrightarrow [SWCNT\text{-}Ni^{2+}]_{film} \quad (4.10)$$

RSH denotes the DEAET, $RS^{\bullet}$ is thiyl radical, while RSSR is the disulphide products. The thiyl ion interact with the SWCNT-confined Ni(II) film forming an adduct, i.e, the adsorption process. Equation 4.8 is assumed to be the rate-determining step which is a one-electron process. The oxidation of the Ni(II) to Ni(III) simultaneously leads to the generation of the $RS^{\bullet}$ which, in turn, undergoes fast and irreversible reaction to form the disulphide product (Equation 4.9). Ni(III) is reduced to regenerate the Ni(II) (Equation 4.10). Given the adsorption phenomenon observed so far, it seems reasonable to assume that adsorption stripping voltammetry is more conceivable than chronoamperometry. To validate this assumption, the electrochemical adsorption equilibrium constant *(β)* was established using the Langmuir Adsorption Isotherm theory [28] below:

$$\frac{[DEAET]}{\Gamma} = \frac{I}{\beta\Gamma} + \frac{[DEAET]}{\Gamma} \quad (4.11)$$

where Γ is the maximum surface coverage. Assuming that the LSV catalytic peak or chronoamperometric transient current (I_{cat}) is proportional to the surface concentration of DEAET, Equation 4.11 may be re-written as:

$$\frac{[DEAET]}{I_{cat}} = \frac{I}{\beta I_{cat}} + \frac{[DEAET]}{I_{cat}} \qquad (4.12)$$

By plotting the ratio of the DEAET concentration to the current response against the concentration of DEAET, β values were estimated from the values of the slopes and intercepts of the linear relation (R^2 = 0.9737 and 0.9887 for LSV and chronoamperometry, respectively), the electrochemical adsorption Gibbs energy change (ΔG^o) was also calculated from Equation 4.13:

$$\Delta G^o = -RT\ln\beta \qquad (4.13)$$

where R and T have their usual meanings. Table 1 presents the ΔG^o and β values obtained for the two techniques. The high negative ΔG^o values further confirm the strong adsorption of DEAET at the SWCNT-Ni film. The value of β can be used to interrogate whether the detection limit obtained in this study is realistic [29]. The β value of LSV is about three magnitudes lower than that obtained for the chronoamperometric data, meaning that LSV is more realistic than chronoamperometry.

It was envisaged that results shown in this work provide some useful insights into the electrochemical response of thiols, DEAET and related degradation products of V-type nerve agents at metal nanoparticle-decorated carbon nanotubes. The adsorptive behavior of

the SWCNT-Ni may be seen as a limitation to ultra-low detection of DEAET (and very likely other related analytes) using the chronoamperometric methodology. Importantly, this work cautions researchers who wish to use this emerging type of CNT-metal nanoparticle electrocatalytic / sensing platform to first establish the adsorption phenomenon with a view to understanding and applying the most appropriate electrochemical technique to be used for reliable analytical parameters.

References

1. M.T. Martınez, M.A. Callejas, A.M. Benito, M. Cochet, T. Seeger, A. Anson, J.Schreiber, C. Gordon, C. Marhic, O. Chauvet, J.L.G. Fierro, W.K. Maser, *Carbon* 41 (2003) 2247.

2. http://www.cem.msu.edu/<reusch/VirtualText/Spectrpy/InfraRed/infrared.htm [accessed on 9 January 2008].

3. Y.Wang, Z. Iqbal, S. Mitra, *J. Am. Chem. Soc.* 128 (2006) 95.

4. M. Pumera, *Langmuir* 23 (2007) 6453.

5. H. Luo, Z. Shi, N. Li, Z. Gu, Q. Zhuang, *Anal. Chem.* 73 (2001) 915.

6. M. Dmochowska, A. Czerwinski, *J. Solid State Electrochem.* 2 (1998) 16.

7. A. Czerwinski, M. Dmochowska, M. Grden, M. Kopczyk, G.Wojcik, G.Młynarek,J. Kołata, J.M. Skowronski, *J. Power Source* 77 (1999) 28.

8. A. Salimi, M. Roushani, S. Soltanian, R. Hallaj, *Anal. Chem.* 79 (2007) 7431.

9. I.D. Raistrick, D.R. Franceschetti, J.R. Macdonald, in: E. Barsoukov, J.R. Macdonald (Eds.), *Impedance Spectroscopy: Theory Experiment, and Applications*, second ed., Wiley, Hoboken, New Jersey, 2005, p. 27.

10. X.Wu, H. Ma, S. Chen, Z. Xu, A. Sui, *J. Electrochem. Soc.* 146 (1999) 1847.

11. G. Nurk, H. Kasuk, K. Lust, A. Janes, E. Lust, *J. Electroanal. Chem.* 553 (2003) 1.

12. C. Hu, X. Dang, S. Hu, *J. Electroanal. Chem.* 572 (2004) 161.

13. T. Thomberg, J. Nerut, E. Lust, *J. Electroanal. Chem.* 586 (2006) 237.

14. E. Bonanos, B.C.H. Steele, E.P. Butler, in: E. Barsoukov, J.R. Macdonald (Eds.), Impedance Spectroscopy: Theory

Experiment, and Applications, second ed, Wiley, Hoboken, New Jersey, 2005, p. 284.

15. J.V. Dobson, B.R. Chapman, *Electrochim. Acta* 32 (1987) 415.

16. K.I. Ozoemena, T. Nyokong, *Inorg. Chem. Commun.* 6 (2003) 1192.

17. C. Zhang, S. M. J. Park, *J. Electrochim. Soc.* 136 (1989) 3333.

18. I.D. Raistrick, D.R. Franceschetti, J.R. Macdonald, in Impedance Spectroscopy: Theory Experiment, and Applications, 2nd ed., (Eds: E. Barsoukov, J. R. Macdonald), Wiley, Hoboken, NJ 2005, ch. 2, p 27.

19. G.D. Christian Analytical Chemistry, 6th ed. John Wiley and Sons New York, 2004, p 113.

20. J.-M. Zen, A. Senthil Kumar, M.-R. Chang, *Electrochim. Acta* 45 (2000) 1691.

21. K.A. Joshi, M. Prouza, M. Kum, J. Wang, J. Tang, R. Haddon, W. Chen, A. Mulchandani, *Anal. Chem.* 8 (2006) 331.

22. O.V. Shulga, C. Palmer, *Anal. Bioanal. Chem*. 385 (2006) 1116.

23. C.L. Copper, G.E. Collins, *Electrophoresis*, 25 (2004) 897.

24. J. Wang, J. Zima, N.S. Lawrence, M.P. Chatrathi, *Anal. Chem.*, 76 (2004) 4721.

25. J. Pillay, K. I. Ozoemena, *Electrochim. Acta* 52 (2007) 3630.

26. J. Pillay, K.I. Ozoemena, *Electrochem. Commun.* 9 (2007) 1816.

27. F. Bedioui, S. Griveau, T. Nyokong, A.J. Appleby, C.A. Caro, M. Gulppi, G. Ochoa, J.H. Zagal, *Phys. Chem. Chem. Phys.* 9 (2007) 3383.

28. H.X. Lu, L. Donal, *J. Electroanal. Chem.* 484 (2000) 150.

29. W. Yang, E. Chow, G.D. Willet, D.B. Hibbert, J.J. Gooding, *Analyst* 128 (2003) 712.